Digital Elevation Models of the Moon from Earth-Based Radar Interferometry

Jean-Luc Margot, Donald B. Campbell, Raymond F. Jurgens, *Member, IEEE*, and Martin A. Slade

***Abstract*—Three-dimensional (3-D) maps of the nearside and polar regions of the Moon can be obtained with an Earth-based radar interferometer. This paper describes the theoretical background, experimental setup, and processing techniques for a sequence of observations performed with the Goldstone Solar System Radar in 1997. These data provide radar imagery and digital elevation models of the polar areas and other small regions at $\sim$100 m spatial and $\sim$50 m height resolutions. A geocoding procedure relying on the elevation measurements yields cartographically accurate products that are free of geometric distortions such as foreshortening.**

***Index Terms*—Interferometry, moon, radar, topography.**

I. Introduction

SEVERAL problems in lunar science and comparative planetology cannot be addressed satisfactorily due to an incomplete knowledge of the topography of the Moon. The difficulties stem mostly from the lack of elevation data over the polar regions and the generally sparse coverage in nonequatorial areas. For instance, current models of global lunar topography [1] must rely on interpolation to fill in missing data at the poles, and this procedure may affect the determination of global shape parameters. The search for ice deposits in cold traps at the lunar poles [2]–[5] is also hampered by the lack of topographic maps in those regions. Finally, interplanet comparisons of impact cratering and the superficial processes that affect impact craters suffer from the lack of an adequate topographic data set for the Moon. While craters on Earth and Mars have been adequately sampled, the coverage for some key craters on the Moon is too sparse to allow detailed crater morphometry.

Spacecraft measurements of lunar topography include vertical metric photography as well as laser altimetry data acquired during Apollo missions 15, 16, and 17 [6]. These measurements were restricted to roughly $\pm 30^\circ$ of latitude, and have absolute errors on the order of 500 m. Additional maps for nonequatorial regions are based on Orbiter IV and V stereo photography, with absolute errors of 500 m or more, depending on the quality of stereoscopic coverage. More recently, the Clementine spacecraft [7] carried a light detection and ranging (lidar) instrument, which was used as an altimeter [1]. The lidar returned valid data for latitudes between 79°S and 81°N, with an along-track spacing varying between a few km and a few tens of km. The across track spacing was roughly 2.7° in longitude or $\sim$80 km at the equator. Because the instrument was somewhat sensitive to detector noise and to solar background radiation, multiple returns were recorded for each laser pulse. An iterative filtering procedure selected 72 548 altimetry points for which the radial error is estimated at 130 m [1].

Detailed topographic maps of the lunar surface, including the polar regions, can be acquired with an Earth-based radar interferometer. The technique is similar to terrestrial topographic mapping from interferometric synthetic aperture radar (SAR) observations and was first described by Shapiro *et al.* [8] and Zisk [9] in 1972. Zisk obtained measurements of lunar topography with the Haystack–Westford radar systems and published results for the Alphonsus–Arzachel region [10] and the Crisium area [11]. The spatial resolution in those experiments was 1–2 km and the elevation accuracy on the order of 500 m. We use radar interferometry with modern instrumentation and processing techniques in order to provide accurate digital elevation models (DEM's) of the Moon with $\sim$100 m spatial and $\sim$50 m height resolutions. Since the original formulation of the technique for lunar mapping, radar interferometry has been applied to terrestrial remote sensing [12] and has been used with considerable success for a variety of geophysical applications [13].

Our description of the basic concept underlying Earth-based radar interferometry closely follows the approach presented in Shapiro *et al.* [9]. Consider an Earth-based radar system and two receiving stations forming an interferometer. The distance between the two interferometer elements, *the baseline* B, is assumed to be much smaller than the range R to the planetary target under consideration. In a typical radar experiment, one records radar echoes in both amplitude and phase in order to extract information about the nature and location of the scattering surface. When a radar interferometer is available, additional information about the location of the reflection elements can be obtained. This comes about because incoming wavefronts have different arrival times at the two receiving antennas. The time delay depends on the orientation of the incident radiation and can be related to the interferometric phase [14] (i.e., the phase difference between the two radar echoes). For example, a 2π phase change is recorded at the interferometer when the orientation of incoming radio waves changes by $\lambda/B_\perp$, where λ is the wavelength and $B_\perp$ is the baseline projected on the plane

Manuscript received February 1, 1999; revised August 30, 1999. This work was supported in part by NASA Grant NAG 5-4220 and by the Jet Propulsion Laboratory, operated by the California Institute of Technology under contract with the NASA.

J.-L. Margot is with the National Astronomy and Ionosphere Center, Arecibo, PR 00612 (email margot@naic.edu).

D. B. Campbell is with the Department of Astronomy, Cornell University, Ithaca, NY 14853 USA.

R. F. Jurgens and M. A. Slade are with the Jet Propulsion Laboratory, California Institute of Technology, Pasadena, CA 91109 USA.

Publisher Item Identifier S 0196-2892(00)02485-2.

perpendicular to the line of sight. At the distance of the Moon, this angular difference corresponds to a *fringe spacing* given by

$$s = R\frac{\lambda}{B_\perp}. \tag{1}$$

Topographic changes on the lunar surface can be related to a measurable interferometric phase because the location of reflection elements in the fringe pattern of the interferometer is elevation-dependent [8]. Height deviations Δz parallel to the projected baseline produce phase changes $\Delta\phi$ at the interferometer in proportion to

$$\frac{\Delta z}{s} = \frac{\Delta\phi}{2\pi} \tag{2}$$

hence

$$\Delta z = R\frac{\lambda}{B_\perp}\frac{\Delta\phi}{2\pi}. \tag{3}$$

For typical fringe spacings ($s \simeq$1 km), this formula shows that elevations can be measured with ∼50 m resolution provided that the interferometer phase can be determined to ∼20°.

II. Imaging and Interferometry in Planetary Radar

A. Delay-Doppler Mapping

High spatial resolution in planetary radar imaging is obtained in much the same way as in terrestrial radar applications. The delay-Doppler algorithm, first suggested by Green [15] and first applied by Pettengill [16], is equivalent to the range-Doppler algorithm, which preceded airborne SAR. Although planetary radar observations usually do not incorporate range cell migration corrections, focused algorithms were developed by Stacy [17] and Webb *et al.* [18] for high resolution imaging of the Moon.

The essence of delay-Doppler mapping is to isolate the backscattered signal from various resolution cells based on their distance (range) and line of sight velocity with respect to the observer. The radar observables are the roundtrip time delay and Doppler frequency shift, with the Doppler shift arising from orbital and rotational motions of the Earth and Moon. The amplitude of the Doppler shift can be expressed simply by defining the *apparent rotation axis*, a vector perpendicular to the line of sight, which represents the apparent angular velocity of the target as seen by the radar.

For convenience in describing the mapping geometry, we introduce a time-dependent coordinate system (**i, j, k**) with origin at the moon's center of mass, a modified version of that described in [8]. The unit vectors **i** and **k** are defined by the line of sight and the apparent rotation axis, respectively. Axis **j** completes the right-handed coordinate system.

As illustrated in Fig. 1, the loci of points at a given time delay (range) from the radar are planes perpendicular to the line of sight direction $\boldsymbol{i}$. The loci of points with a constant Doppler frequency are planes parallel to the line of sight direction $\boldsymbol{i}$ and to the apparent rotation axis $\boldsymbol{k}$. Analysis of the radar echoes in time delay and Doppler frequency therefore measures radar backscatter from different parts of a target.

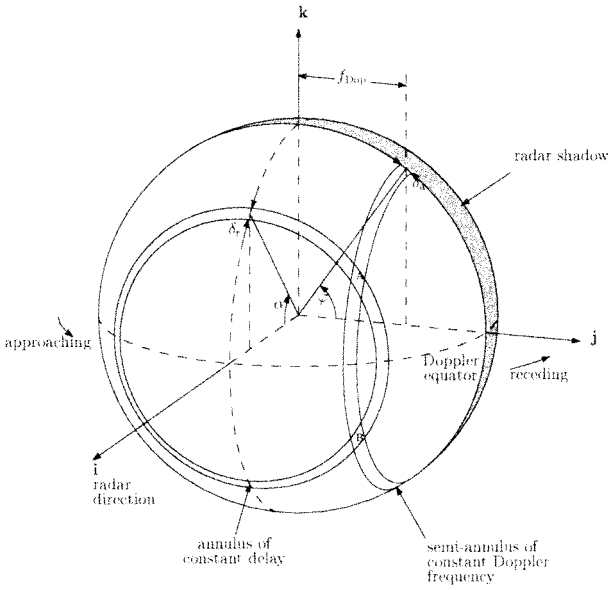

Fig. 1. Delay-Doppler mapping geometry. The loci of points at a given time delay from the radar are planes perpendicular to the line of sight direction $\boldsymbol{i}$, which are shown to intersect the sphere as a grey annulus. The loci of points with a constant Doppler frequency are planes parallel to the line of sight direction $\boldsymbol{i}$ and to the apparent rotation axis $\boldsymbol{k}$ and are shown to intersect the sphere as a white semi-annulus. Two resolution elements, one on each side of the Doppler equator, have the same delay and Doppler values, giving rise to a North–South ambiguity. Adapted from Stacy [17].

In the case of a nearly spherical body such as the Moon, the delay and Doppler loci take the form of annuli, as shown in Fig. 1. Two resolution cells on the surface have equivalent delay and Doppler values, such that their echo powers combine and are indistinguishable in a delay-Doppler map. This condition is called the "North–South ambiguity." When observing nearby objects, this problem can be alleviated by the selectivity offered by the antenna beam pattern. If one illuminates a region far from the Doppler equator, the contribution from associated points in the other hemisphere is negligible, provided that the antenna footprint is much smaller than the target diameter. For more distant celestial objects, the antenna beam may not resolve the two hemispheres, and another solution to the ambiguity problem must be found. For instance, Roger and Ingalls [19] used a radar interferometer in order to obtain unambiguous images of Venus. By analyzing the signals at both receive antennas, they were able to separate contributions from points on both hemispheres. Their use of an interferometer was not related to the measurement of elevations, but later extensions of the technique [20], [21] did provide altitude contours.

The delay and Doppler values of a reflection element at position $\boldsymbol{r}$ can be expressed with respect to the delay and Doppler values of the center of mass (COM). The difference in roundtrip delay is given by

$$\tau_{\mathrm{sr}} = -\frac{2}{c}(\boldsymbol{r}\cdot\boldsymbol{i}) \tag{4}$$

where c is the speed of light. If $\boldsymbol{\omega} = \omega \boldsymbol{k}$ represents the apparent rotation axis of the Moon, the Doppler shift with respect to the COM is given by

$$f_{\mathrm{Dop}} = \frac{2}{\lambda} |\boldsymbol{\omega} \times \boldsymbol{r}| \cdot \boldsymbol{i} = -\frac{2}{\lambda} \omega (\boldsymbol{r} \cdot \boldsymbol{j}). \tag{5}$$

We now present estimates of the spatial resolution that can be achieved with the delay-Doppler technique. Resolution in the range direction depends on the pulse duration. If the transmitted pulse can be compressed into a short pulse of length $\delta\tau$, the resolution along $\boldsymbol{i}$ (the delay direction) is

$$\delta_{\mathrm{sr}} = \frac{c}{2} \delta\tau. \tag{6}$$

This is the usual *slant range resolution*, with the corresponding ground resolution given by $\delta_r = \delta_{\mathrm{sr}} / \sin \alpha$, where α is the incidence angle.

Resolution in the Doppler dimension is achieved by spectral analysis of the returned echoes. The spectral resolution $\delta\nu$ is given by the inverse of the time interval over which radar returns are collected. The resolution along the Doppler direction $\boldsymbol{j}$ is therefore

$$\delta_{\mathrm{Dop}} = \frac{\lambda}{2\omega} \delta\nu. \tag{7}$$

The actual ground resolution is given by $\delta_a = \delta_{\mathrm{Dop}} / \sin \varphi$, where φ is the Doppler angle as defined in Fig. 1.

B. Three-Dimensional (3-D) Mapping

Analysis of the radar echoes in time delay and Doppler frequency constrains the position of reflection elements in two dimensions. If a suitable interferometer is available, the location of surface elements along the third dimension (elevation) can be measured. The previous section showed that points with given delay and Doppler values lie at the intersection of two orthogonal planes. These delay-Doppler lines are parallel to the apparent rotation axis $\boldsymbol{k}$ and are intersected by the fringe pattern of the interferometer, as shown in Fig. 2. A measure of the interferometric phase ϕ (i.e., the phase difference recorded by the two receivers forming the interferometer), can therefore be used to determine the elevation of each delay-Doppler resolution cell.

Fig. 2 shows an arbitrary reflection element located at $\boldsymbol{r} + \boldsymbol{\delta r}$. In the mapping procedure, one seeks estimates of the position $\boldsymbol{r}$ (possibly expressed as a latitude and longitude) and elevation $|\boldsymbol{\delta r}|$ above a reference ellipsoid. We now outline how these quantities can be measured from the observables: delay τ, Doppler frequency f, and interferometric phase ϕ.

Solving the problem is facilitated by the introduction of an imaginary point at position $\boldsymbol{r'}$, with the same delay and Doppler values as the reflection element at position $\boldsymbol{r}$. This point is chosen to be at zero elevation, and its imaginary interferometric phase ϕ_0 can therefore be computed from ephemeris data.

The distance $|\boldsymbol{r} + \boldsymbol{\delta r} - \boldsymbol{r'}|$ along the direction $\boldsymbol{k}$ can be derived from the difference between the measured phase ϕ at position $\boldsymbol{r} + \boldsymbol{\delta r}$ and the computed phase ϕ_0 at position $\boldsymbol{r'}$. This phase

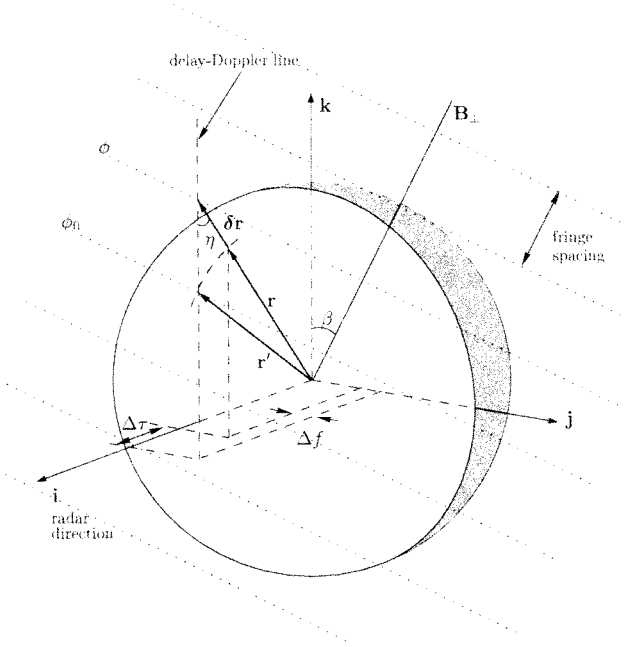

Fig. 2. Interferometric phase measurements in the context of the delay-Doppler imaging geometry. The projected baseline of the interferometer $\boldsymbol{B}_\perp$ lies in the plane perpendicular to the line of sight $\boldsymbol{i}$ and forms an angle β with the apparent rotation axis $\boldsymbol{k}$. The fringe pattern of the interferometer (i.e., the loci of points with equal fringe phase) is shown with dotted lines. The height of the reflection element $|\boldsymbol{\delta r}|$ induces changes $\Delta\tau$ and Δf in the delay and Doppler coordinates compared to those of a point at the same latitude and longitude but at zero elevation.

difference is shown to be equivalent to a fringe spacing for ease of drawing in Fig. 2. The general relation is

$$|\boldsymbol{r} + \boldsymbol{\delta r} - \boldsymbol{r'}| = \frac{(\phi - \phi_0)}{2\pi} \frac{s}{\cos \beta} \tag{8}$$

where s is the fringe spacing and β is the angle between the projected baseline $\boldsymbol{B_\perp}$ and the apparent rotation axis $\boldsymbol{k}$. Projection along the normal to the ellipsoid yields the height $|\boldsymbol{\delta r}|$

$$|\boldsymbol{\delta r}| = |\boldsymbol{r} + \boldsymbol{\delta r} - \boldsymbol{r'}| \cos \eta. \tag{9}$$

In this last transformation, the required angular separation between the normal $\boldsymbol{r}$ and direction $\boldsymbol{k}$ is not known *a priori*. A very good estimate of the angle η is given by the separation between $\boldsymbol{r'}$ and $\boldsymbol{k}$. This approximation is legitimate since topographic changes represent a very small fraction of the planetary radius, and $\boldsymbol{r'}$ is expected to be nearly aligned with $\boldsymbol{r}$. The approximation breaks down at low incidence angles in a region where radar imaging is avoided because of ambiguity difficulties.

The height $|\boldsymbol{\delta r}|$ above the sphere is assigned to the delay-Doppler coordinates of the reflection element under consideration. Note that these delay and Doppler values are different from those of a zero-elevation point located at the same latitude and longitude, as illustrated in Fig. 2. A coordinate transformation between delay-Doppler space and latitude-longitude space would therefore result in geometric distortions (e.g., foreshortening) if it did not take the topography into account.

The process of registering a radar map to a specific cartographic projection with due account for the elevation-induced distortions is called *geocoding* or *rectification*. The required corrections to the delay and Doppler values can be computed from a knowledge of the elevation $\boldsymbol{\delta r}$. They parallel (4) and (5)

$$\Delta\tau = \frac{2}{c}(\boldsymbol{\delta r}\cdot\boldsymbol{i}) \tag{10}$$

$$\Delta f = \frac{2}{\lambda}\omega(\boldsymbol{\delta r}\cdot\boldsymbol{j}). \tag{11}$$

These corrections can be implemented to produce digital elevation models and radar images, which are properly rectified and free of elevation-induced distortions.

A final note about the mapping procedure is in order. In the derivation of (8) and (9), we have assumed that the phase ϕ is a measure of the absolute path difference between a reflection element and the two receiving stations. In reality, this absolute value is unknown, and the actual phase measurements $\hat{\phi}$ are offset from the true value by some arbitrary, constant amount $\delta\phi$. The conversion to heights therefore proceeds according to

$$|\boldsymbol{\delta r}| = \frac{(\hat{\phi}-\phi_0)}{2\pi}\frac{s}{\cos\beta}\cos\eta + \frac{\delta\phi}{2\pi}\frac{s}{\cos\beta}\cos\eta. \tag{12}$$

All the quantities in this equation can be measured or computed with the exception of the phase offset $\delta\phi$. This parameter can be evaluated by comparing the radar data to surface control points of known absolute elevation.

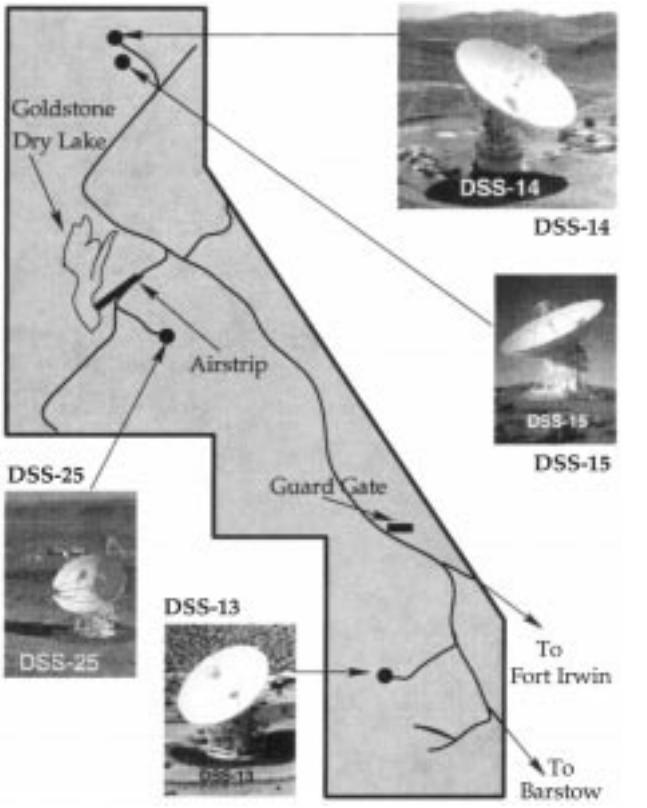

Fig. 3. Deep Space Network-Goldstone antenna locations. Courtesy NASA/JPL.

III. Observational Parameters

A. Interferometer Configuration

The data were obtained at X-band ($\lambda = 3.5$ cm, $\nu = 8510$ MHz) with the antennas of the Deep Space Network (DSN) at Goldstone, CA. The 70 m parabolic dish (DSS-14) was used to transmit, and two or three 34-m antennas (DSS-13 / DSS-15 / DSS-25), separated by 10–20 km formed the receive interferometers. Equation (1) shows that such baselines result in fringe spacings on the order of 1 km. Antenna locations are shown in Fig. 3.

B. Observing Times

As indicated by (8), the best height resolution for a given precision in the phase measurements is obtained when the projected baseline of the interferometer is parallel to the apparent rotation axis ($\beta = 0$). Observing times were selected in order to match this condition as closely as possible.

When mapping the lunar polar regions, viewing conditions also constrain the choice of adequate observing times. Since the spin axis of the Moon is inclined by 6.7° with respect to its orbital plane, an observer on Earth will view slightly different aspects of the Moon during the lunar cycle. These *latitude librations* can be quantified simply in terms of the motion of the subradar point (SRP) (i.e., the point closest to the radar on the lunar ellipsoid). Subradar point latitude variations are approximately sinusoidal with a period similar to the lunar cycle and an amplitude of ∼7°. The best Earth-based views of the lunar poles occur when this function reaches its extrema. In such a geometry, the radar rises ∼7° above the horizon at the lunar poles. In comparison, the limb of the Sun never rises by more than 1.8° above the same horizon. Note that these viewing conditions imply extreme incidence angles ranging from 80 to essentially 90°. For this reason, Earth-based radar images of the lunar polar regions contain a significant fraction of radar shadow.

TABLE I
Observing Times (UT hr:mn) for Radar Observations of the South Pole on October 6, 1997 and the North Pole on October 19, 1997. BOT: Begining of Track; EOT: End of Track; and SRP: Subradar Point Latitude (Degrees). The Numbers Describing the Baseline Refer to the Antennas used for the Interferometer, DSS-13, DSS-15, and DSS-25

Date	BOT	EOT	SRP	β	Baseline
Oct 06	20:30	22:10	-6.1	0.1 – 39.1	13 - 25
Oct 19	11:00	13:30	+7.0	37.2 – 30.1	13 - 25
Oct 19	11:00	13:30	+7.0	24.5 – 20.1	13 - 15

Table I lists observing times for the North and South pole observations.

C. Data Coverage

Limits to the spatial extent of radar images were dictated by the field of view of the instrument. The beam pattern of the 70 m antenna, with a full width at half maximum of 1.8 arcminutes, defined ∼200 km footprints on the lunar surface. Near the limb of the Moon however, the antenna footprint takes an elongated shape, and the useful range extent can be substantially larger.

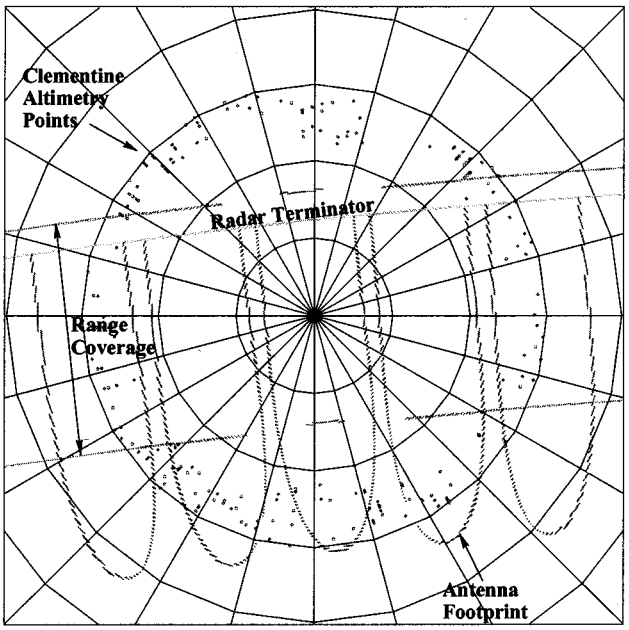

Fig. 4. Data coverage in the lunar polar regions. The figure represents the view for an observer looking down at the pole, with the zero of longitude (the average Earth direction) toward the bottom and latitude lines drawn at 5° increments. The radar terminator represents points illuminated by the radar at 90° incidence angle. Five footprints are defined by the intersection of the antenna power pattern at the 3 dB level with the surface. The range extent of each one of the five images is also shown. The locations of Clementine altimetry measurements poleward of 75° are indicated by black dots and illustrate the lack of topographic data in the polar regions.

When imaging the polar regions, coverage along the range dimension was typically 375 km and up to 450 km, but these upper bounds were set by data rate limitations rather than by beam considerations.

Our observations of the lunar polar regions were designed to obtain elevation maps down to latitudes of 70°, where the radar-derived topography can be linked to existing Clementine altimetry measurements [1]. This objective required assembling five individual maps into ∼1200 km wide mosaics of the polar regions. The precise arrangement of the pieces of the mosaic is shown in Fig. 4.

D. Polarization

Transmitted waveforms were circularly polarized. The receivers were set to the opposite sense of circular polarization for DSS-15 and DSS-25, but both senses of circular polarization were recorded at DSS-13. Although single polarization measurements are sufficient for topographic mapping, dual polarization capability provides a valuable tool in the search for ice deposits, as icy bodies in the solar system exhibit unusual polarization properties [22].

E. Sensitivity

As illustrated by (5), good range resolution implies the use of narrow pulses. This requirement potentially conflicts with high SNR for the radar echoes, because radar transmitters cannot supply arbitrary amounts of power in a short time. To circumvent this problem, we used the common technique of pulse compression, which allows us to transmit the energy contained in a long pulse while still achieving the resolution given by a short pulse.

TABLE II
GOLDSTONE DATA COLLECTION PARAMETERS

peak transmitter power	$P_{\rm t}$	350 kW
transmitter antenna gain	$G_{\rm t}$	74 dB
distance to Moon	R	3.8×10^8 m
backscatter cross-section	σ	-30 dB
receiver antenna effective area	$A_{\rm r}$	580 m^2
receiver system temperature	$T_{\rm sys}$	30 K
noise temperature of Moon	$T_{\rm moon}$	200 K
compressed pulse width	$\delta\tau$	0.5 μs
uncompressed pulse width	τ_p	2 ms
pulse repetition frequency	f_p	32 Hz
coherent processing interval	$t_{\rm coh}$	250 s

The SNR for a pulsed waveform is

$$\mathrm{SNR} = \frac{P_{\rm t} G_t}{4\pi R^2} \sigma A_{\rm scatt} \frac{A_{\rm r}}{4\pi R^2} \frac{1}{kTB} \frac{\tau_p}{\delta\tau} f_p t_{\rm coh} \qquad (13)$$

where

- $P_{\rm t}$ peak transmitter power;
- G_t transmitter antenna gain;
- R distance to the Moon;
- σ surface backscatter cross section per unit surface area;
- $A_{\rm scatt}$ area of the resolution cell;
- $A_{\rm r}$ effective area of the receive antenna;
- k Boltzmann's constant;
- T sum of the receiver system temperature and the noise temperature contribution from the Moon;
- B bandwidth of the receiving system;
- τ_p uncompressed pulse width;
- $\delta\tau$ compressed pulse width;
- f_p pulse repetition frequency;
- $t_{\rm coh}$ coherent processing interval.

This is the usual radar equation [23], modified to include the compression factor $\tau_p/\delta\tau$ and the coherent processing of a number $f_p t_{\rm coh}$ of pulses. Note that in this equation, $B\delta\tau \approx 1$ and $\tau_p f_p$ is the radar *duty cycle* (i.e., the ratio of pulse width to pulse repetition period).

An estimate of the SNR can be obtained with the parameters listed in Table II. For a 75×75-m resolution cell with a backscatter cross section of -30 dB, the SNR is roughly 16 dB. The backscatter cross section of -30 dB is the cross section of the Moon measured at 85° incidence angle and 3.8 cm wavelength [24].

The requirements on sensitivity were driven by the desire to obtain adequate phase accuracy across the imaged areas. Interferometric phase estimates are corrupted by noise in the measurement of radar backscatter. The probability distribution of phase errors was computed by Vinokur [25] and approaches a Gaussian distribution with standard deviation $\sigma_\phi \simeq 60°/\mathrm{SNR}$ for large values of the SNR. Our experiment was designed such

that the SNR would remain sufficient to yield phase accuracies on the order of 10°, even past the 3 dB point of the primary beam (Fig. 4). This dictated the use of fairly long (uncompressed) pulses in order to ensure high SNR.

The waveform parameters listed in Table II yield a set of reasonable values for interferometric topographic mapping of the Moon. The height resolution that can be expected on the basis of a 20° accuracy in the phase measurements and km-type fringe spacings is about 50 m, commensurate with the spatial resolution. SNR estimates indicate that such phase accuracies represent a realistic goal with the use of ∼2 ms pulse widths. Additionally, spatial resolutions of 75 m gives many resolution cells per fringe spacing, which allows one to track phase variations smoothly from one surface element to the next.

F. Resolution in Range and Frequency

Range discrimination was achieved by using binary phase code modulation [26], in which the phase of the transmitted waveform alternates between 0–180° according to a pseudo-random sequence (maximal-length shift register codes). The length of the sequence (*code length*) was 4095, and the time interval of each code element (*baud length*) was $0.5\ \mu$s, resulting in a range resolution of 75 m.

A total of 8192 pulses acquired over a period of ~ 250 s were processed coherently to yield a frequency resolution $\delta\nu$ of ~ 0.004 Hz. This gives a cross-range resolution of 75 m, either by using (7) or by comparing the frequency resolution to the total Doppler broadening of the Moon $4\omega R_m/\lambda$. In this equation, R_m is the 1738 km lunar radius, and the apparent rotation rate of the Moon is on the order of 10^{-6} rad s^{-1}, resulting in a limb-to-limb bandwidth of 180 Hz at X-band.

G. Pulse Repetition Frequency

Imaging requirements placed tight constraints on the parameters of the transmitted waveform. The selection of the pulse repetition frequency f_p was primarily dictated by the need to avoid range and frequency aliasing in the delay-Doppler map.

Range aliasing occurs when the pulse repetition frequency is so high that several pulses illuminate different parts of the scene at the same time. This ambiguity was avoided by making sure that successive pulses were separated by a duration greater than the roundtrip light-travel time corresponding to a lunar hemisphere (i.e., $2R_m/c = 11.6$ ms).

Because delay-Doppler mapping requires spectral analysis of the radar echoes for cross-range resolution, frequency aliasing can occur if the Nyquist sampling criterion is not satisfied. A lower bound on the pulse repetition frequency was therefore given by the Doppler bandwidth of the illuminated area, which is on the order of 30 Hz. This represents the product of the total Doppler broadening of the Moon by the fraction of the lunar disk illuminated by the main lobe of the 70-m antenna.

The pulse repetition period $T_p = 1/f_p$, typically between 28–32 ms, was chosen as an integer multiple of the ∼2 ms pulse width. An additional constraint came from the requirement that radar echoes for the region of interest should return during the transmitter-off time. Since the range to the Moon changes continuously, a particular value of the pulse repetition period would remain adequate for a limited period of time, 1–2 h at the most.

Radar returns were recorded for roughly 5 ms periods interleaved with the transmitted pulses. The precise location of the data acquisition window in the pulse train was constantly adjusted by drifting clocks according to ephemeris information. Compensating for the Earth–Moon motion in such a way ensured that data records from separate pulses sampled the same region on the surface of the Moon.

H. Demodulation

Phase coherence was maintained throughout the system by using a single frequency standard. All local oscillators in the frequency converters were controlled by a master 5 MHz clock, which is part of the DSN's frequency and timing subsystem. Data from receiver stations were delivered to the DSS-14 control room using links with carriers at 50 MHz intermediate frequency (IF). Baseband conversion was accomplished with complex mixers that provided in-phase (I) and quadrature (Q) components. A 0.5 μs matched filter was used before A/D conversion of the raw voltage samples.

I. Sampling Timebases

Separate PC-based data acquisition systems were used to record samples from the various receiving antennas. Each unit was individually clocked at a rate that was continuously updated based on precomputed ephemeris polynomials. The different nonuniform timebases were required because the Earth–Moon motion affects the length of the pulse and the pulse repetition period in the returned echo. This effect depends on the relative target-receiver velocity, and hence antenna location. In order to keep the sampling in step for all receiving stations, data were sampled with separately drifted clocks.

J. Differential Delay and Doppler Corrections

Similarly, antenna-specific time delays and Doppler shifts were applied to ensure that echoes from the center point of the illumination would register at a unique position in delay-Doppler space, irrespective of antenna location. The differential Doppler corrections were read from precomputed ephemeris polynomials and applied via programmable local oscillators. Differential delay values were incorporated into the system that provided drifted sampling clocks. The latter system also accounted for different propagation times from each receiver to the DSS-14 control room, (i.e., differential link delays).

In practice, the bulk of these corrections were applied upon transmission, so that the received waveform at one antenna was sampled without any modifications. The transmitted frequency was continuously adjusted to force the received passband at the master receiving antenna to be centered at exactly 8510 MHz. Timebase drifting was also applied on transmission so that a uniform 0.5μs sampling interval could be used at the master receiving antenna. Other receiving antennas were corrected for the differential effects in delay, Doppler, and sampling times.

IV. Processing Techniques

A. Image Formation

Conventional delay-Doppler mapping [27] involves a range (delay) compression step followed by a cross-range (Doppler) compression operation.

Processing in range relied on the fact that binary phase-coded waveforms have very sharply peaked autocorrelation functions [26]. Range compression consisted in correlating each data record with a replica of the transmitted code. This operation, known as "decoding," was performed with Fourier transform techniques, as described in [17]. Because the autocorrelation function of the 4095 code has sidelobe levels at -34 dB of the peak, and the lunar backscattering function at X-band extends over $\sim$30 dB [24], range sidelobes from bright regions are sometimes visible in the imagery.

Resolution in the across-range (Doppler) dimension was achieved by spectral analysis of consecutive radar returns. This was implemented as a fast Fourier transform (FFT) on 2^n consecutive samples for each range value. The resulting two-dimensional (2-D) array of complex numbers formed the required delay-Doppler image. Complex images were formed independently for each receiving antenna.

The conventional delay-Doppler mapping technique works well, as long as individual resolution cells do not migrate appreciably in delay-Doppler space during data collection. If range or frequency migration is significant (compared to the size of a resolution cell), the delay-Doppler image will exhibit some blurring, in which case, focused algorithms [17], [18] can be used to improve image quality. For interferometric applications, defocusing also causes decorrelation of the image pair and a degradation of the phase measurements.

In most planetary radar imaging scenarios, one arranges for the image center to appear at zero delay and Doppler. This is accomplished by tracking the trajectory of a designated center point through delay-Doppler space and by removing its delay-Doppler time history from the entire data set. Therefore, the central region of a delay-Doppler map is usually well focused, with cell migration effects most noticeable near the image boundaries. Indeed, the criterion for deciding on the usefulness of a focused algorithm is based on a measure of the defocusing expected at the map edges.

For the Goldstone lunar observations, the region of interest within each map was never more than $r \simeq 150$ km away from the image center point. The ensuing maximum cell migration $\delta r = \omega t_{\mathrm{coh}} r$ was only a fraction of the resolution cell size, which suggests that conventional delay-Doppler mapping techniques were adequate.

B. Image Coregistration

Interferometric phase measurements require very precise alignment of the interferometric image pair. Resampling operations were performed to ensure that images obtained at different receiving stations would properly register to one another. The amplitude of the required pixel shifts were found by implementing the algorithm described in Gabriel and Goldstein [28].

This method relies on the idea that interference fringes have the highest quality when the images are correctly aligned. The technique consists of iteratively shifting one image with respect to the other and obtaining a 2-D Fourier transform of the interference pattern at each iteration. The fractional pixel shifts that result in power spectra with sharply defined peaks are the best candidates for large fringe visibility, and hence, properly registered images.

In reality, the search is carried out at many subimage patches across the image, in order to capture variations in the required pixel offsets. The line and sample pixel offsets are then fitted with a polynomial that provides adequate pixel shifts across the entire image for the resampling operation.

C. Interferogram Formation

After proper registration of image pairs, their complex product $s = s_1 \times s_2^*$ was obtained pixel by pixel, and this provides an estimate of the interferometric phase at each resolution cell. Modest filtering of the interferogram was used in order to reduce phase noise. As pointed out by Goldstein *et al.* [29], the selection of filter weights must take into account the existing fringe pattern present in the image. A simple low-pass filter cannot be applied, as it would smear out the phase information and reduce the quality of the fringes.

At this stage of the processing, the phase function contains two distinct components: a large contribution due to the curvature of the lunar surface, and a smaller contribution due to local topographic variations superimposed on that surface. Since only the latter is of interest, we removed the phase component due to a reference surface from the interferogram. This operation of *interferogram flattening* was accomplished by computing the expected interferometric phase of a reference ellipsoid at every pixel location, and by applying the corresponding phase rotation. Residual phases represent topographic variations with respect to the chosen reference ellipsoid, in this case, a sphere of radius 1738 km.

D. Phase Unwrapping

Because lunar height variations exceed the km-type fringe spacing available in our experiments, several 2π phase cycles are required to record the full range of topographic expression. However, an interferometer can only measure phases modulo 2π, and this results in an ambiguity in the height determination. A variety of *phase unwrapping* techniques exist to circumvent this problem. These algorithms track phase deviations over the image and add multiples of 2π as necessary to preserve continuity. We used the well-known method of Goldstein *et al.* [29] to unwrap phases from their $[0, 2\pi]$ representation into a continuous phase function spanning several cycles. This algorithm and other phase unwrapping techniques are extensively reviewed elsewhere [30].

Because radar maps of the lunar poles were acquired at extreme incidence angles, the images contain a significant fraction of radar shadow, where meaningful phase estimates cannot be obtained. The digital elevation models in those areas are therefore incomplete. In regions of poor coherence, unwrapping algorithms may fail. Error recognition is usually straightforward,

(a)

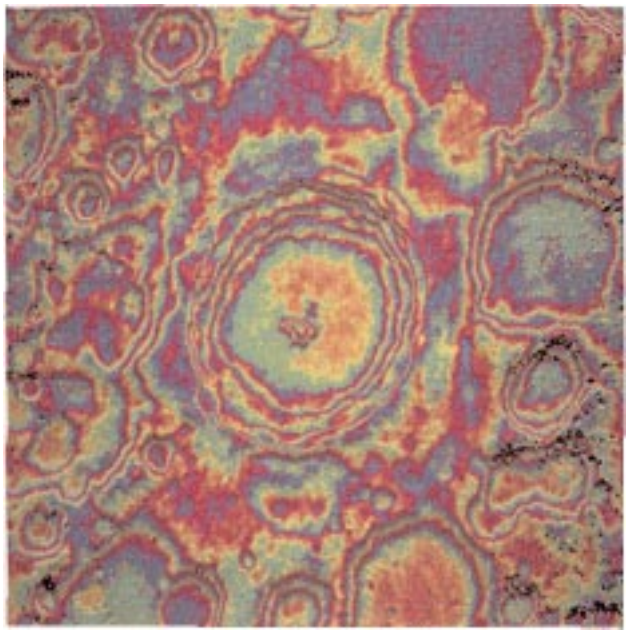

(b)

Fig. 5. (a) Radar backscatter map of the Tycho region. The image is in delay-Doppler coordinates, with time delay (range from the observer) increasing top to bottom and Doppler frequency increasing to the left and (b) interferogram corresponding to the same area. The spacing between identical colors represents 360° of phase, or an elevation difference of 1290 m.

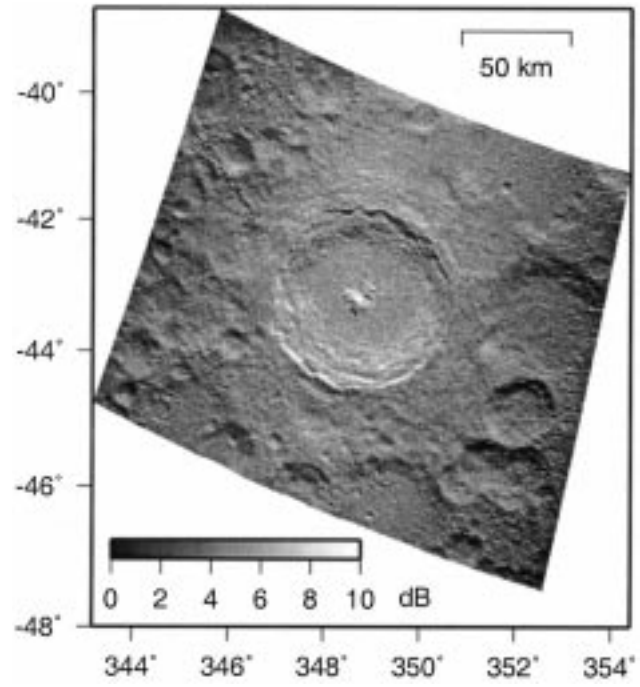

(a)

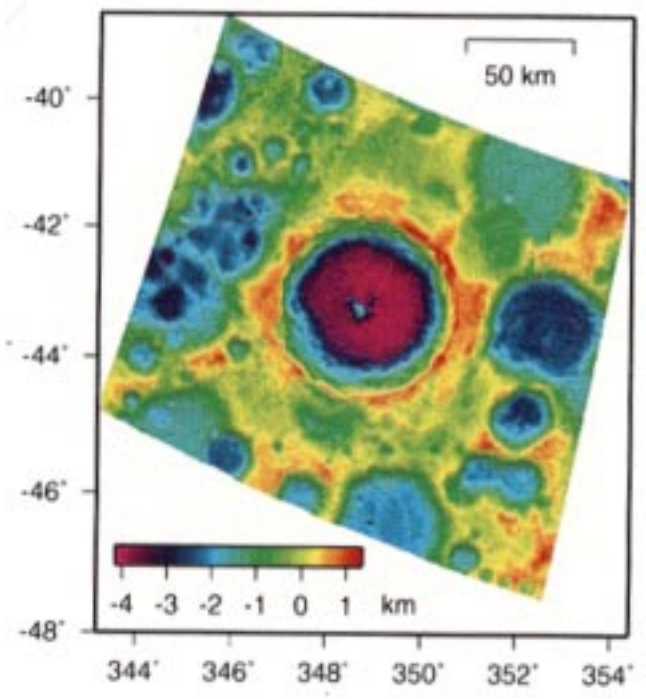

(b)

Fig. 6. (a) Rectified radar imagery of Tycho Crater shown in a Mercator projection, with east longitude on the horizontal axis. An arbitrary logarithmic scale is used to represent differences in radar backscatter and (b) digital elevation model of the same region. Heights displayed in the elevation map are from −4100 to +1300 m with respect to a 1738 km radius sphere.

and we compared data from two independent baselines whenever feasible to locate and extract problematic areas.

E. Phase to Height Conversion

Conversion of the unwrapped phases into meaningful topographic variations required a position-dependent scaling operation. This was performed according to (8) and (9).

Absolute heights with respect to the reference sphere were obtained by removing a constant phase offset over the entire map. This offset affects the calculation of elevations through the second term in (12). The amplitude of the required shift was obtained by tying the radar-derived heights to all available Clementine laser altimetry points [1] located in the unshadowed areas, except for obvious outliers.

F. Geocoding

Cartographic projections of the radar maps were obtained by computing the mapping between delay-Doppler coordinates and latitude-longitude coordinates. Since this mapping is affected by topography as indicated in Section II-B, we computed elevation-dependent corrections prior to resampling the data whenever a complete digital elevation model was available. Equations (10) and (11) were then used to provide the required corrections. This geocoding operation was applied to both the imagery and the elevation data.

G. Slope Removal

Comparison of our digital elevation models with Clementine altimetry points revealed that small residual slopes are present in the radar data. The slopes typically have an amplitude of $\sim 0.07^\circ$ and occur mostly along the range direction. Their origin is unknown. A large-scale slope was removed from the radar DEM's to provide the best match with Clementine altimetry points. In the polar regions, where control points are available only along one edge of the imaged area, the errors on absolute heights could arguably become as large as the product of the slope and the range extent (i.e., $\sim$200 m).

V. Results

A. Tycho Crater

The 85-km diameter crater Tycho (43°S, 349°E), the youngest large crater on the Moon, was imaged on October 19, 1997. A 200 $\times$ 200-km delay-Doppler image of the Tycho region is shown in Fig. 5(a). Radar illumination is from the top of the image, as evidenced by the stronger radar return of the radar-facing inner wall of Tycho.

A map of the interferometric phase for the same area is shown in Fig. 5(b). The figure illustrates residual phase deviations obtained after removal of the phase due to a reference 1738 km radius sphere. In this interferogram, the fringe phase of each resolution element was color coded, and the amplitude of the radar backscatter was used to modulate the brightness of each pixel. Flat areas stand out as they exhibit a uniform phase.

Mercator projections of the radar backscatter and elevation data are displayed in Fig. 6(a) and (b), respectively. Note that typical distortions present in radar imagery (such as foreshortened slopes and asymmetry in the crater shape) have been effectively removed by the rectification process described earlier. Correcting geometric distortions shifted the position of elevated features away from the observer, since those features are closer in range than equivalent points at zero elevation. Similarly, pixels with negative elevations were displaced toward the observer so that they would not masquerade as distant features in the projected image. The largest corrections occurred for the deep floor of Tycho, which was translated by $\sim$3 km, compared to its position in the raw radar image.

The digital elevation model shown in Fig. 6(b) was obtained by using two antennas separated by 10 km, such that a 360° phase change at the interferometer determines elevation differences of 1290 m. A separate elevation map (not shown) was constructed independently by using a different combination of receive antennas with a full phase cycle corresponding to a spacing of 675 m.

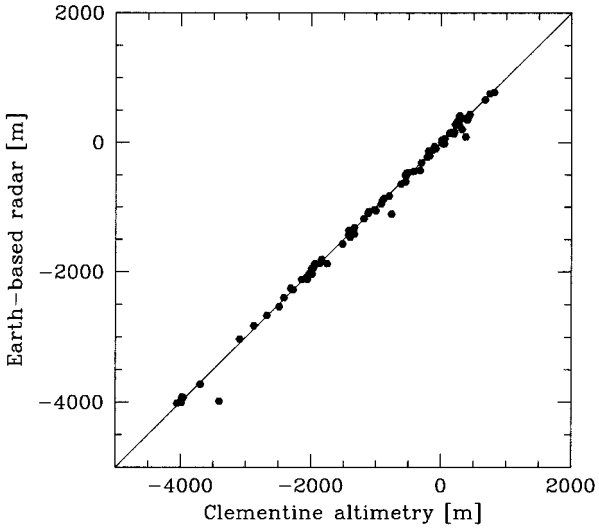

Fig. 7. Comparison of all 87 Clementine altimetry points located across the Tycho scene with the radar-derived topography.

Resolution estimates for the elevation data can be obtained from (2). The expected accuracy in interferometric phase measurements $\Delta\phi$, which depends on the SNR as described earlier, is roughly 10–15°. The corresponding height resolution is on the order of 30 m. We verified that this resolution had indeed been achieved in two different ways. First, we examined heights over presumably flat areas such as crater floors, and obtained rms deviations of roughly 30 m. This tends to indicate that the height resolution is better than 30 m, as a fraction of this value is certainly due to real topography. Second, we compared two elevation maps over the entire 40 000 km^2 scene and found that the rms deviations between them was 45 m. As the maps were obtained independently of each other, this value again argues for individual height resolutions on the order of 30 m for each map.

A comparison of the radar-derived topography data around Tycho with 87 existing lidar altimetry points from the Clementine mission [1] is shown in Fig. 7. The rms deviations between the two data sets is $\sim$90 m. Although not a comparison of completely independent points due to the phase tie described in Section IV-E, this rms measure is a good indicator of the agreement between the two techniques. Detailed analysis of the topography in this region reveals that the worst case discrepancy of 600 m is clearly associated with an erroneous laser altimetry measurement. Two additional suspicious lidar data points differ from both radar topographic maps by $\sim$300 m in elevation.

The radar DEM's represent significant improvements in the description of the topography of the Tycho region in terms of both accuracy and resolution. This provides unprecedented potential for geological interpretations of the crater. For instance, the suggestion [31] that the crater may have resulted from an oblique impact bears on properties that can be directly quantified from the radar map. These features include asymmetries in the crater shape, such as central peak offset, differences in the width of the wall slump zone, and rim height variations. Another diagnostic feature is the increased flow debris over some parts of the crater floor, which is readily observed on the radar DEM

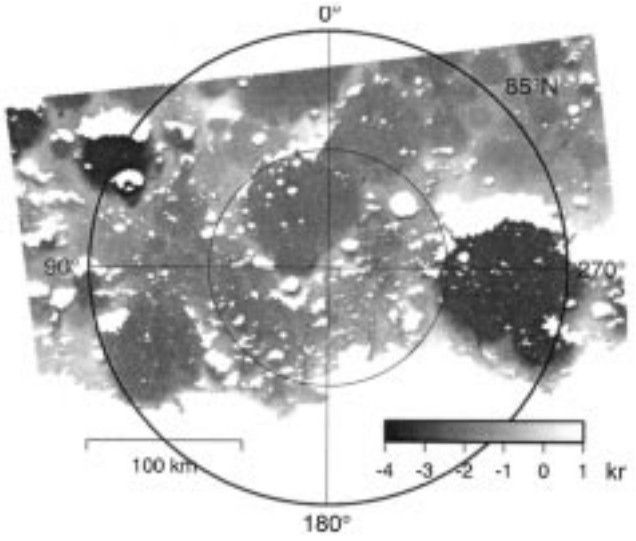

(a)

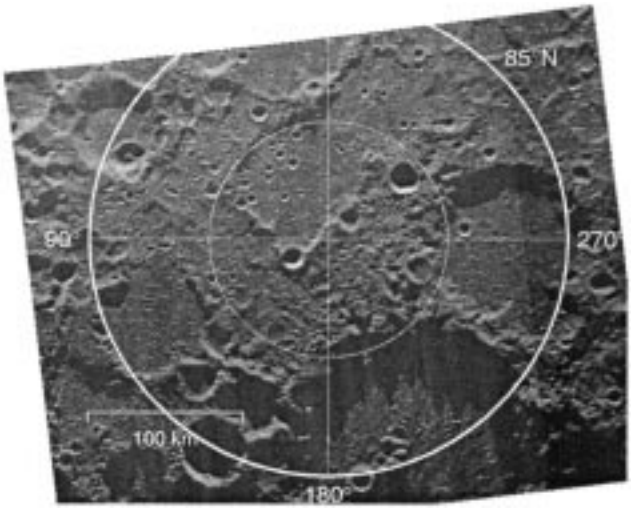

(b)

Fig. 8. Digital elevation model and radar backscatter map of the north polar region. Absolute elevations with respect to a 1738 km radius sphere are shown. Maps are stereographic projections and use east longitudes.

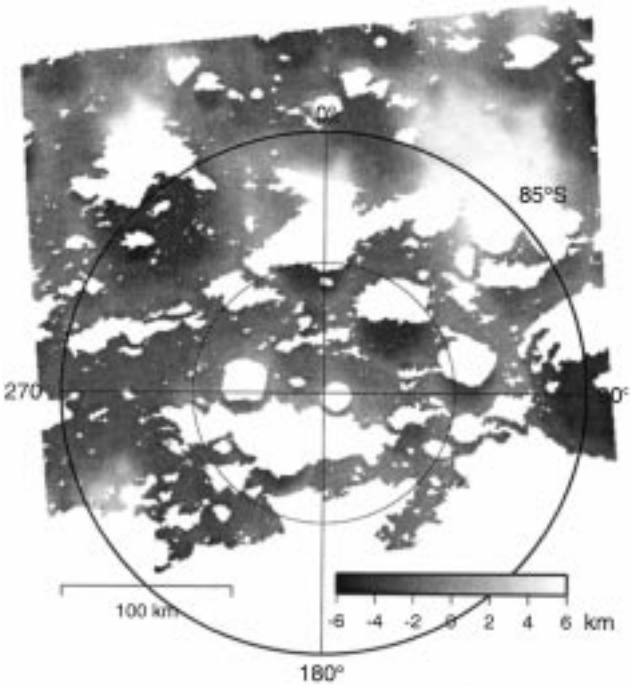

(a)

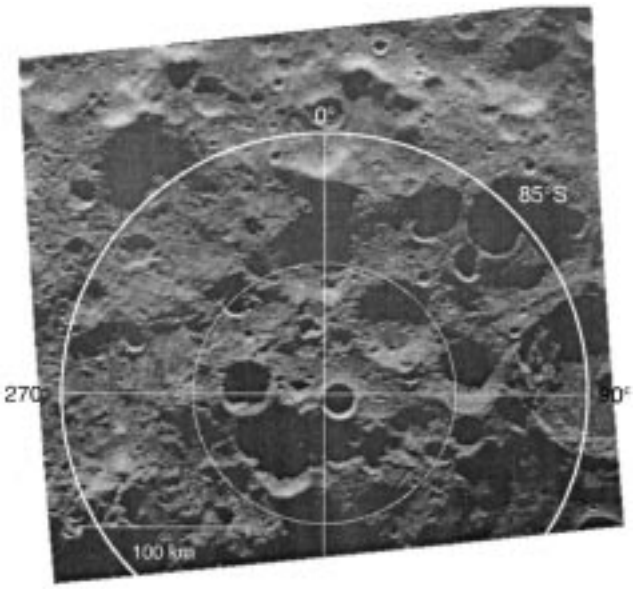

(b)

Fig. 9. Digital elevation model and radar backscatter map of the south polar region. Absolute elevations with respect to a 1738 km radius sphere are shown. Maps are stereographic projections and use east longitudes.

by a measurable dichotomy in floor elevations. Further analysis of the Tycho DEM is provided in [32].

B. Polar Regions

An important objective of our observations was to map the lunar polar areas. The topography in those regions was essentially unknown, since the Clementine laser altimetry data set did not cover latitudes poleward of 80° [1]. However, elevation maps of the lunar polar regions were needed for several studies, including those related to the possible presence of frozen volatiles in regions of permanent shadow. Using an Earth-based radar also offered the ability to map many regions that appeared in shadow on optical images [7].

Topographic maps of the lunar polar regions, shown in Figs. 8 and 9, were obtained at a spatial resolution of 150 m and a height resolution of ∼50 m via Earth-based radar interferometry. The viewing geometry at the time of our observations was such that the radar line of sight rose 6–7° above the horizon at the lunar poles, close to the maximum allowed by the Earth–Moon geometry. At these angles, a fraction of the lunar landscape in the field of view was not illuminated by the radar due to shadowing effects. It was not possible to determine the altitudes of those areas of radar shadow.

The north polar area displays relatively little topographic expression, while the south polar region presents much more

rugged terrain. The range of elevations characterizing the south pole region is roughly 2.5 times that at the north. This may be related to the south polar region being near the rim of the South Pole/Aitken basin, a 2500 km diameter impact structure on the lunar far side.

The digital elevation models were used to simulate solar illumination conditions over the polar regions and to identify the lunar cold traps, possible reservoirs of ice deposits [33]. The simulations showed that the fraction of sun-shadowed regions is significantly higher at the south pole. This finding presents a potential inconsistency with data from the Lunar Prospector spacecraft [5], which detected larger amounts of hydrogen, a tracer for water ice, at the north pole.

VI. Conclusions

Earth-based radar interferometry is a powerful technique for the measurement of lunar topography. The technique can produce geometrically rectified maps at spatial resolutions of $\sim$100 m and height resolutions on the order of 50 m. Absolute elevation levels with respect to a reference ellipsoid can be obtained by comparing the heights with existing ground control points. The radar digital elevation models represent significant improvements over existing topographic data sets for many parts of the Moon and provide an important tool for geological interpretation. With a few hours of antenna time, the Goldstone Solar System Radar provided the first detailed topographic maps of the lunar polar areas and an accurate digital elevation model of the Tycho region.

Acknowledgment

The authors wish to thank R. Goldstein and H. Zebker for providing their phase unwrapping algorithm, C. Werner, R. Goldstein, and S. Zisk for stimulating discussions about radar interferometry, F. Djuth and J. Elder for assistance with the data acquisition, the Navigation and Ancillary Information Facility, Pasadena, CA, for providing an excellent ephemeris toolkit, M. Standish for generating comparison ephemerides, L. Bracamonte for assistance with RF and timing signals, C. Franck for building range-coding equipment, and R. Winkler, P. Dendrenos, R. Rose, D. Choate, D. Kelley, J. Garnica, G. Bury, G. Farner, R. Littlefair, C. Snedeker, and C. Franck for assistance with the observations.

References

[1] D. E. Smith, M. T. Zuber, G. A. Neumann, and F. G. Lemoine, "Topography of the moon from the Clementine lidar," *J. Geophys. Res.*, vol. 102, pp. 1591–1611, Jan. 1997.

[2] S. Nozette, C. L. Lichtenberg, P. Spudis, R. Bonner, W. Ort, E. Malaret, M. Robinson, and E. Shoemaker, "The Clementine bi-static radar experiment," *Science*, vol. 274, pp. 1495–1498, 1996.

[3] R. A. Simpson and G. L. Tyler, "Reanalysis of Clementine bistatic radar data from the lunar South Pole," *J. Geophys. Res.*, vol. 104, pp. 3845–3862, 1999.

[4] N. J. S. Stacy, D. B. Campbell, and P. G. Ford, "Radar mapping of the lunar poles: A search for ice deposits," *Science*, vol. 276, pp. 1527–1530, June 1997.

[5] W. C. Feldman, S. Maurice, A. B. Binder, B. L. Barraclough, R. C. Elphic, and D. J. Lawrence, "Fluxes of fast and epithermal neutrons from lunar prospector: Evidence for water ice at the lunar poles," *Science*, vol. 281, pp. 1496–1500, 1998.

[6] W. M. Kaula, G. Schubert, R. E. Lingenfelter, W. L. Sjogren, and W. R. Wollenhaupt, "Apollo laser altimetry and inferences as to lunar structure," in *Lunar Planet. Sci. Conf.*, vol. 5, 1974, pp. 3049–3058.

[7] S. Nozette *et al.*, "The Clementine mission to the moon: Scientific overview," *Science*, vol. 266, pp. 1835–1839, Dec. 1994.

[8] I. I. Shapiro, S. H. Zisk, A. E. E. Rogers, M. A. Slade, and T. W. Thompson, "Lunar topography: Global determination by radar," *Science*, vol. 178, pp. 939–948, 1972.

[9] S. H. Zisk, "A new, earth-based radar technique for the measurement of lunar topography," *The Moon*, vol. 4, pp. 296–306, 1972.

[10] ——, "Lunar topography : First radar-interferometer measurements of the Alphonsus-Ptolemaeus-Arzachel region," *Science*, vol. 178, pp. 977–980, 1972.

[11] ——, "Mare Crisium area topography; A comparison of Earth-based radar and Apollo mapping camera results," *Geochim. Cosmochim. Acta*, pp. 75–80, 1978.

[12] H. A. Zebker and R. M. Goldstein, "Topographic mapping from interferometric synthetic aperture radar observations," *J. Geophys. Res.*, vol. 91, pp. 4993–4999, Apr. 1986.

[13] R. Gens and J. L. Van Genderen, "Review article: SAR interferometry-issues, techniques, applications," *Int. J. Remote Sensing*, vol. 17, no. 10, pp. 1803–1835, 1996.

[14] M. Born and E. Wolf, *Principles of Optics*, 6th ed. New York: Pergamon, 1980.

[15] P. E. Green, Jr, "Radar astronomy symposium report," *J. Geophys. Res.*, vol. 65, pp. 1108–1115, 1960.

[16] G. H. Pettengill, "Measurements of lunar reflectivity using the Millstone Radar," *Proc. IRE*, vol. 48, pp. 933–934, 1960.

[17] N. J. S. Stacy, "High-resolution synthetic aperture radar observations of the Moon," Ph.D. dissertation, Cornell Univ., Ithaca, NY, 1993.

[18] J. L. H. Webb, D. C. Munson Jr., and N. J. Stacy, "High-resolution planetary imaging via spotlight-mode synthetic aperture radar," *IEEE Trans. Image Processing*, vol. 7, pp. 1571–82, Nov. 1998.

[19] A. E. E. Rogers and R. P. Ingalls, "Radar mapping of Venus with interferometric resolution of the range-doppler ambiguity," *Radio Sci.*, vol. 5, pp. 425–433, Feb. 1970.

[20] H. C. Rumsey, G. A. Morris, R. R. Green, and R. M. Goldstein, "A radar brightness and altitude image of a portion of Venus," *Icarus*, vol. 23, pp. 1–7, Sept. 1974.

[21] R. F. Jurgens, R. M. Goldstein, H. R. Rumsey, and R. R. Green, "Images of Venus by three-station radar interferometry—1977 results," *J. Geophys. Res.*, vol. 85, pp. 8282–8294, Dec. 1980.

[22] D. B. Campbell, J. F. Chandler, S. J. Ostro, G. H. Pettengill, and I. I. Shapiro, "Galilean satellites—1976 radar results," *Icarus*, vol. 34, pp. 254–267, May 1978.

[23] M. I. Skolnik, *Introduction to Radar Systems*, 2nd ed, ser. Elect. Eng. New York: McGraw-Hill, 1980.

[24] T. Hagfors, "Remote probing of the Moon by infrared and microwave emissions and by radar," *Radio Sci.*, vol. 5, pp. 189–227, 1970.

[25] M. Vinokur, "Optimization dans la recherche d'une sinusoide de période connue en présence de bruit," *Ann. d'Astrophys.*, vol. 28, no. 2, pp. 412–445, 1965.

[26] F. T. Ulaby, R. K. Moore, and A. K. Fung, "Microwave remote sensing: Active and passive," in *Radar Remote Sensing and Surface Scattering and Emission Theory*. Reading, MA: Addison-Wesley, 1982, vol. II.

[27] J. V. Evans and T. Hagfors, Eds., *Radar Astronomy*. New York: McGraw-Hill, 1968.

[28] A. K. Gabriel and R. M. Goldstein, "Crossed orbit interferometry: Theory and experimental results from SIR-B," *Int. J. Remote Sensing*, vol. 9, no. 5, pp. 857–872, 1988.

[29] R. M. Goldstein, H. H. Zebker, and C. L. Werner, "Satellite radar interferometry: Two-dimensional phase unwrapping," *Radio Sci.*, vol. 23, no. 4, pp. 713–720, 1988.

[30] D. C. Ghiglia and M. D. Pritt, *Two-Dimensional Phase Unwrapping: Theory, Algorithms, & Software*. New York: Wiley, 1998.

[31] P. H. Schultz and R. R. Anderson, "Asymmetry of the Manson impact structure; evidence for impact angle and direction," in *The Manson Impact Structure, Iowa: Anatomy of an Impact Crater*, C. Koeberl and R. R. Anderson, Eds. New York: Geolog. Soc. Amer., 1996.

[32] J. L. Margot, D. B. Campbell, R. F. Jurgens, and M. A. Slade, "The topography of Tycho Crater," *J. Geophys. Res.*, vol. 104, pp. 11 875–11 882, May 1999.

[33] ——, "Topography of the lunar poles from radar interferometry: A survey of cold trap locations," *Science*, vol. 284, pp. 1658–1660, 1999.

Jean-Luc Margot received the B.S. degree in electrical engineering from the University of Louvain, Louvain, Belgium, and the Ph.D. degree in astronomy and space sciences from Cornell University, Ithaca, NY.

He is currently a Research Associate at the Arecibo Observatory, Arecibo, PR, where he is involved in planetary studies and remote sensing. He has previously worked on the measurement of atmospheric water content from microwave observations and on characterizing the lunar regolith via multiwavelength polarimetric radar and radio observations. His current research interests include the study of scattering from planetary surfaces, the use of radar interferometry for topographic mapping and surface change detection, and the inversion of delay-Doppler data for shape reconstruction. He is also pursuing the implementation of two-element radar interferometry techniques for the unambiguous imaging and the three-dimensional characterization of small bodies.

Donald B. Campbell received the B.S. and M.S. degrees in physics from the University of Sydney, Sydney, Australia, and the Ph.D. degree in astronomy and space sciences from Cornell University, Ithaca, NY.

From 1971 to 1987, with one brief interruption, he was a Member of the scientific staff of the Arecibo Observatory, Arecibo, PR, serving as Director of the Observatory from 1982 to 1987. In 1988, he was appointed Professor of Astronomy at Cornell University and in 1993, he was appointed Associate Director of the National Astronomy and Ionosphere Center, which operates the Arecibo Observatory. His research work has centered primarily on the study of the radio wavelength scattering properties of the surfaces of the planets and smaller bodies in our solar system.

Dr. Campbell is a member of AGU, URSI, and AAS.

Raymond F. Jurgens (S'58–M'61) received the B.S. and M.S. degrees in electrical engineering in 1959 and 1963, respectively, from Ohio University, Athens. In 1968, he received the Ph.D. degree in electrical engineering and space science from Cornell University, Ithaca, NY.

From 1965 to 1970, he was a Resident at the Arecibo Observatory, Arecibo, PR, where he was involved in the planetary radar program and the first radar mapping of the planet Venus. From 1970 to 1972, he was an Associate Professor at Ohio University, Athens. Since 1972, he has been with the Jet Propulsion Laboratory, Pasadena, CA, and has been involved in projects ranging from the heliogyro to the Vega balloons. However, the majority of his effort has been devoted to the development of the Goldstone Solar System Radar Facility, Goldstone, CA. His scientific work is primarily related to the imaging of Venus and the analysis of asteroids.

Dr. Jurgens is a Member of IEEE, AAS, IAU, and URSI.

Martin A. Slade received the S.B. and S.M. degrees in physics, and the Ph.D. degree in earth and planetary sciences, all from the Massachusetts Institute of Technology, Cambridge.

He is the Group Supervisor of the Planetary Radar Group in the Communications Systems and Research Section, Jet Propulsion Laboratory, Pasadena, CA, and is also Manager of the Goldstone Solar System Radar (GSSR) Task, Goldstone, CA. He has previously worked in the area of very long baseline interferometry and also in the area of modeling of crustal deformation using the finite element technique. He has made radar observations using the Haystack Observatory, Arecibo Observatory, Arecibo, PR, and the VLA, in addition to the GSSR, which operates from the 70-m antenna of the deep space network in California.

Dr. Slade is a Member of AGU, AAS, and Commission 19 (Earth Rotation) of the IAU.